SAND2015-0331C 96

Experimental and Numerical Investigations of Close-Coupled Pilot Injections to Reduce Combustion Noise in a Small-Bore Diesel Engine

Author, co-author (Do NOT enter this information. It will be pulled from participant tab in MyTechZone)

Affiliation (Do NOT enter this information. It will be pulled from participant tab in MyTechZone)

Abstract

A pilot-main injection strategy is investigated for a part-load operating point in a single cylinder optical Diesel engine. As the energizing dwell between the pilot and main injections decreases below 200 µs, combustion noise reaches a minimum and a reduction of 3 dB is possible. This decrease in combustion noise is achieved without increased pollutant emissions. Injection schedules employed in the engine are analyzed with an injection analyzer to provide injection rates for each dwell tested. Two distinct injection events are observed even at the shortest dwell tested; rate shaping of the main injection occurs as the dwell is adjusted. High-speed elastic scattering imaging of liquid fuel is performed in the engine to examine initial liquid penetration rates. The penetration rate data provide evidence that rate shaping of the initial phase of the main injection is occurring in the engine and that this rate shaping is largely consistent with the injection rate data, but the results demonstrate that these changes are not responsible for the observed trend in combustion noise.

A zero-dimensional model is created to investigate the causes of the observed combustion noise behavior. The trend in simulated combustion noise values agree well with the experimentally determined trend, which is associated with two main factors: relative changes in combustion phasing of the pilot and main heat release events and suppression of the pilot apparent heat release for dwell times near the minimum-noise dwell. Two possible mechanisms by which the relative phasing between the pilot and the main heat release events impacts combustion noise are proposed.

Introduction

Pilot injections have long been used in direct injection Diesel engines as a means to reduce combustion noise [1,2]. The mechanism by which noise is reduced is as follows: the heat released by the pilot fuel increases temperatures and radical concentrations within the cylinder and therefore decreases the ignition delay of the fuel injected during the main injection. Consequently, heat release rates during the main portion of the combustion are predominantly mixing-controlled and smaller in magnitude than for premixed combustion. The relatively small amount of pilot fuel, combined with the interruption in the rate of injection, results in a smaller amount of premixed combustion than for a single injection. In this way, combustion noise is suppressed through the use of a pilot. Advances in fuel injection hardware, such as common rail systems and fast response injectors, have made multiple injection strategies robust and effective. Piezo injectors are well known for their precision and short reaction times, but state-of-the-art solenoid injectors can reliably deliver up to eight injections per cycle with very short separation times between injection events [3]. Split armature modules enable closely spaced injections and even zero hydraulic dwell (delay) between injection events. With this system, injection rate shaping is possible [3, 4]. Various definitions of dwell can be found in the literature, but for this study, dwell refers to the time between the end of the pilot energizing signal and the beginning of the main energizing signal (see Figure 1).

Dürnholz *et al.* investigated the effects of a pilot injection on combustion noise, fuel economy, and emissions with various pump-line-nozzle injector configurations in a passenger car Diesel engine of unspecified displacement [2]. Their injection system made it possible to vary the quantity, timing, and rate of the pilot injection. For an engine speed of 2000 rpm and a “medium” load, combustion noise depended strongly on the pilot quantity; minimal combustion noise levels were achieved with a pilot quantity of between 2 and 3 mm^3/str. The noise minimum corresponds to a minimum in ignition delay for the main injection, and to approximately 8% of the fuel being burned before the start of the main injection. Measured combustion noise was always lower with a pilot than without, but the noise increased for hydraulic dwells (injection interrupt durations) shorter than approximately 12 °CA (1000 µs at 2000 rpm).

Badami *et al.* performed investigations using a common rail system with solenoid injectors in a passenger car Diesel engine [5]. They examined three different operating points with pilot-main injection strategies and varied pilot injection quantity and energizing dwell at each point. At a fixed load, pilot injection quantity affected not only the combustion noise at a given energizing dwell, but also the trend in combustion noise with changing dwell. Moreover, trends in combustion noise with changing dwell for different operating points were quite different for a given pilot injection quantity. At moderate engine loads (bmep/n: 5 bar/1500 rpm and 8 bar/2000 rpm), combustion noise sometimes changed dramatically for energizing dwells shorter than 500 µs. At the highest load tested (8 bar/2000 rpm) and for the larger pilot injection quantities tested, combustion noise was observed to decrease dramatically at the shortest energizing dwells (near 86 µs). Badami *et al.* show that by varying only the dwell for a given pilot injection quantity, combustion noise can vary by as much as 3 dB; this is equivalent to a factor of 2 in acoustic power.

Ricaud and Lavoisier optimized multiple injection settings in a single-cylinder, small-bore engine with a piezoelectric injector for

several multiple injection strategies [6]. Dwell and quantity were varied for each injection event, as well as the start of the main injection, the rail pressure, and the EGR rate. For a pilot-main injection strategy, combustion noise varied significantly as dwell and pilot injection quantity were changed. Furthermore, the pilot fuel quantity resulting in the lowest combustion noise level depended on the dwell. The noise-optimal pilot injection quantity was smallest for intermediate dwells. For noise-optimized operation, peak heat release rates are the same for the pilot and the main combustion events. This observation was made for several operating points, and it was suggested that the noise-optimized settings are a balance between excessive pilot heat release and excessive main combustion heat release.

Properly applied multiple injection strategies can be beneficial for combustion noise, fuel consumption, and pollutant emissions, and are therefore a powerful tool. However, with so many calibration parameters, including injection and dwell durations for each injection event; rail pressure; and injection train phasing; developing engine calibrations over the entire operating map is a complicated and time consuming process. A particular injection train may yield minimal combustion noise for a given operating point, but it may not be obvious why these parameters are optimal or why different parameters are necessary for a different operating point. Without a detailed understanding of the mechanisms by which noise can be decreased with multiple injections and closely coupled pilot injections, it will be difficult to reduce the amount of effort necessary to develop and optimize such calibrations. The goal of this work is to investigate the effects of energizing dwell time on combustion noise with a pilot-main injection strategy and to describe the mechanisms responsible for the observed trend in combustion noise.

In this study, a pilot-main injection strategy is investigated at moderate load in an optical small-bore Diesel engine. The pre-production injector used is a fast-acting, pressure-balanced, solenoid-actuated injector, which enables very closely coupled injection events. Engine testing is performed for a dwell sweep at a moderate load, and trends in exhaust emissions, heat release rates, and combustion noise are measured. The injection schedules used in the engine testing are measured with a hydraulic injection analyzer to provide rate shapes for each of the dwells tested. High speed elastic scattering images are taken in the engine to provide information about liquid fuel penetration and penetration rate behavior for several dwells. A zero-dimensional computational model is implemented to systematically provide insight about the observed trends in combustion noise and their relation to injection behavior and heat release phasing.

Experimental Setup and Procedures

Engine and Fuel Injector

The single-cylinder optical Diesel engine used in this study is based on a modified General Motors cylinder head with four valves per cylinder. The production version of this engine has four cylinders and a displacement of 1.9 L. The main geometric specifications are provided in Table 1. The engine features a Bowditch-style piston, which is fitted either with a titanium piston top for cylinder pressure and emissions measurements; or with a fused-silica piston top for the optical investigations described below. The geometrically identical piston tops feature a reentrant bowl and valve cut-outs.

Table 1: Engine geometry and fuel properties

Valves	4
Bore	82 mm
Stroke	90.4 mm
Displacement volume	0.477 L
Geometric compression ratio	16.7 : 1
Fuel	58 vol% 2,2,4,4,6,8,8-heptamethylnonane (iso-$C_{16}H_{34}$); 42 vol% n-hexadecane (n-$C_{16}H_{34}$)
Cetane number	50.7

Optical access through the sides of the combustion chamber is provided by fused silica windows (50 mm width, 25 mm height) located at the top of the cylinder liner. These windows are positioned to allow unobstructed optical access into the clearance volume, even when the piston is located at top dead center (TDC). The engine is equipped with a Kistler 6125b pressure transducer, which is mounted in place of the glow plug. The cylinder pressure is digitized every 0.25 crank angle degrees (CAD).

A blend of the diesel reference fuels, *n*-hexadecane and heptamethylnonane, was used in this study. This blend has been chosen to match the ignition delay and physical properties of conventional diesel fuel more closely than the blend of n-heptane and isooctane used previously [7], and has been used in more recent studies [8, 9]. Its cetane number of 50.7 is calculated from the relationship given by Heywood [10].

The fuel injector used in this study is a pre-production solenoid-based injector, which is equipped with a pressure-balanced nozzle control valve to enable very closely spaced injection events. The mini sac nozzle has equally spaced holes with exit diameters of 139 µm; the included angle of the holes is 149°. Flexible control of solenoid energizing durations (referred to as ET) and energizing dwells was provided by a Genotec injector controller. The dwell was varied between 80 and 1200 µs.

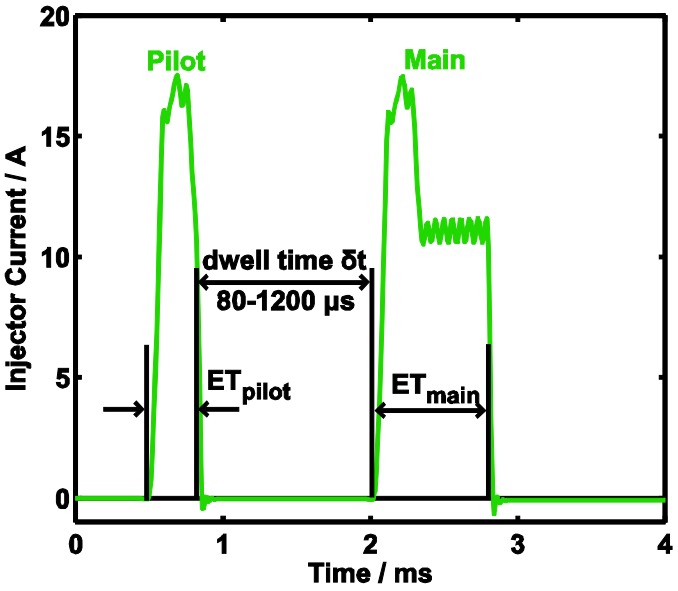

Figure 1: injector solenoid energizing and dwell definition

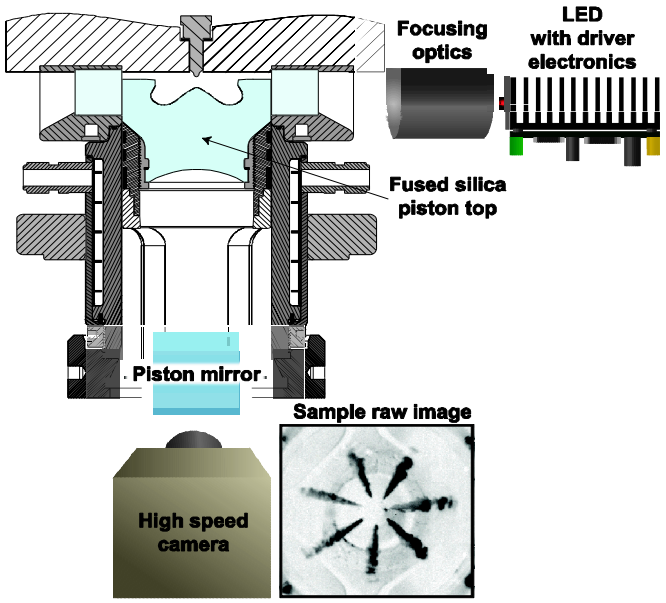

Figure 2: Setup for high speed elastic scattering imaging and sample raw image (inverted grayscale color map, 0-512 counts, gamma = 0.7)

Fuel Injection Rate Measuring Device

Rates of injection were measured with the same fuel injection hardware used in engine testing, but with the injector mounted in a Moehwald HDA rate and quantity measuring device [11]. The HDA utilizes the change in hydraulic pressure that occurs when fuel is injected into a constant volume, pressurized, fuel-filled chamber. Additionally, the speed of sound of the fuel in the chamber is measured before and after each injection train. Injection mass flow rates and quantities are then computed from the chamber pressure and speed of sound measurements. The measurement hardware, working principle, and experimental setup are described in more detail in [12].

Fuel Injection Imaging Setup

An elastic scattering imaging technique was developed to provide temporally and spatially resolved information about the fuel injection process in the motored engine. An evaluation of the dynamic liquid fuel penetration behavior provided a qualitative check of injection rates measured with the HDA to verify trends in main injection rate shapes as dwell changes. Imaging was performed with a Photron SA-X2 monochromatic CMOS camera at a frame rate of 120 kfps; this provides adequate temporal resolution (0.075 CAD at 1500 rpm) of the pilot and main injection events for even the shortest dwells. Images were captured through the bottom of the fused silica piston with a Nikkor lens (focal length: 105 mm, aperture: f/3.5). The cylinder head and valves were airbrushed with a thin coat of matte black heat resistant paint to reduce reflections. A high repetition rate, high intensity, short pulse LED illumination system was employed to provide sufficient image intensities at these high frame rates. A red LED with a 3x3 mm^2 chip proved to be robust and sufficiently bright with a pulse duration of 1.5 µs, using a peak forward current exceeding 45 A. The LED pulses were timed so that the exposure of each camera frame began approximately 1 µs before the LED pulse and ended several microseconds after the pulse. A system of three plano-convex lenses was developed to increase the amount of light that was passed into the cylinder. The setup in the test bench including the "focusing optics" is depicted in Figure 2 along with an example of a raw image.

The LED and its lens system were positioned outside of the liner window on the intake side of the engine. The incoming light is scattered by the strong density gradients at the fuel jets, and the angle of incidence relative to the jet axis is different for each jet. This non-axisymmetric illumination can complicate the image analysis, but each jet is treated independently in the image processing. Errors associated with non-uniform illumination are negligible in comparison to the changes observed with changing dwell. The trigger to start acquiring images is the signal used to trigger the injector driver to start injecting, i.e. it occurs at the start of solenoid energizing (SSE). In each injected cycle, 300 images are taken to capture the entire pilot and main injection events. Images are taken for 45 consecutive (skip-fired) cycles for each dwell tested.

The raw images are distortion corrected with an automated routine based on ray tracing; background subtracted using the approximate median method to model the background; and thresholded before liquid penetration lengths and penetration rates are computed from them. These procedures are described in the Appendix, where an example of a processed image is also shown.

Experimental Procedures

Initial testing was performed with the metal piston to characterize the fired operation of the engine for a variation of dwell. For these tests, the engine was operated with a constant engine speed; $IMEP_g$, injection pressure; and pilot injection quantity (see Table 2). The engine was operated in skip-fire mode: fuel was injected in every fifth cycle. The main injection duration was adjusted to maintain the engine load ($IMEP_g$), and the injection train was block-shifted to achieve a near-constant 50% mass fraction burned angle (MFB50) of 13 CAD ATDC. EGR was simulated by replacing intake air with a mixture of nitrogen and CO_2 and matching the total mass in the cylinder to the mass that would be present with real EGR. The residual fraction that would be expected in a continuously fired metal engine was also simulated in this manner. The mass flow rate of intake gas was held constant throughout the testing and resulted in a

gas density of approximately 21.8 kg/m^3 at TDC for motored operation. Exhaust emissions (NO_x, smoke number, CO, and UHC) were measured during skip-fired operation and corrected to represent emissions levels obtained in continuously-fired operation. For each operating point, the engine was motored for approximately 90 seconds to allow the intake and exhaust pressures to stabilize. An emissions measurement was taken just before the engine was skip-fired and subtracted from the subsequent skip-fired measurement; a second emissions measurement was taken after approximately 60 seconds of skip-fired operation and averaged over 20 seconds of operation. This procedure removes background emission levels and mitigates the effects of instrument drift, so the resulting values can be attributed to the combustion. The methodology by which emissions values are computed is briefly discussed in [13].

Table 2: Engine operating parameters

Engine speed	1500 rpm
Swirl ratio (Ricardo)	2.2
Intake pressure	1.51 bar
Intake temperature (measured in runner)	353 K
EGR rate (simulated)	10.3% (includes 3.3% residual fraction)
[O_2] (intake)	19.7
Intake gas flowrate	8.5 g/s
TDC temperature	925 K
TDC density	21.8 kg/m^3
Injection pressure	800 bar
m_{pilot}	1.5 mg 0 (single)
m_{main}	22.1-24.5 25.9 (single)
Dwell time δt for initial testing δt…*step size*… δt	0 (no pilot) 80…*20*…200 µs 300…*100*…500 µs 600…*200*…1200 µs
Dwell time δt for optical measurements	0, 90, 140, 300 µs
$IMEP_g$	9.0 ± 0.1
MFB50	13 ± 0.5 CAD ATDC

After the initial engine testing, the injector was tested in the HDA. Rates of injection were measured for the injection schedules developed during the engine testing, among others. The HDA chamber pressure was set to be consistent with the cylinder pressure at the time of injection. Fuel and chamber temperatures were held constant at 90°C, although measured rates of injection are not sensitive to fuel temperature at temperatures above 60°C.

The injector was then reinstalled in the engine and the fused silica piston top was installed. Intake air mass flow was replaced with pure nitrogen to prevent combustion and the associated window fouling. The CO_2 flow rate was left unchanged. Four of the injection trains developed in fired operation were used for the optical measurements.

For each fired operating point (measured with the metal piston), combustion noise is calculated for each of 50 cycles of unfiltered cylinder pressure data according to the routine provided in [14]. This routine computes a fast Fourier transform of the cylinder pressure trace, filters the resulting spectrum to represent structural attenuation by the engine and the frequency response (A-weighted) of the human ear, and integrates the resulting filtered spectrum. This integrated value is normalized by the threshold of human hearing (20 µPa) to provide combustion noise in dB(A). All combustion noise values reported in this work are computed in this manner. The reader is referred to [14] for more details, but this routine is similar or identical to the routines used by commercial devices to compute combustion noise. The average of these 50 values is reported here for each case.

Apparent heat release rate (AHRR) is computed with an iterative, two-zone model, in which temperature and composition dependent gas properties are taken into account. Heat transfer and crevice flow effects are partially compensated by subtracting the AHRR of a motored pressure trace from the AHRR of the fired trace. The AHRR traces shown in this work are ensemble averaged over 50 fired cycles. A cosine-symmetric low pass FIR filter is used to smooth the fired cylinder pressure traces before the AHRR is calculated. Its pass band edge is located at 5 kHz. This preserves the frequency content of the cylinder pressure traces in the frequency bands most relevant to combustion noise. The cylinder pressure spectral data shown in this work have been filtered with a structural attenuation filter and a A-weighting filter (both are given in [14]), then divided by the threshold of human hearing, and expressed in dB(A). The resulting spectra are referred to as a sound pressure level. The amplitude of the sound pressure level is a measure of each frequency component's contribution to audible combustion noise.

Zero-Dimensional Modeling

A zero-dimensional computational model was constructed to aid in understanding the observed trends in combustion noise. This model makes it possible to decouple changes in the heat release rate from changes in the combustion phasing, which is typically not possible in the fired engine. A heat release rate profile (heat release rate vs. crank angle) is either artificially created or derived from measured data and given as an input to the model. Based on this heat release profile, the resulting cylinder pressure trace (including the gas exchange process) is computed. Combustion noise is computed from the simulated cylinder pressure trace using the routine described above. The computation of the cylinder pressure trace from an arbitrary heat release profile is described below.

The first law of thermodynamics for a control volume in differential form can be expressed as:

$$dU = dQ - dW + \dot{m}_i h_i - \dot{m}_e h_e \quad (1)$$

dU is the differential of the total internal energy of the control volume

dW is the differential boundary work

$\dot{m}_i$ and $\dot{m}_e$ are the mass flow rates into and out of the control volume, respectively

h_i and h_e are the specific enthalpies of the intake and exhaust flows, respectively

dQ is given by:

$$dQ = dQ_{HR} - dQ_{wall} \quad (2)$$

dQ_{HR} is the pre-defined heat release rate and the primary simulation input

dQ_{wall} is the heat loss to the walls, and is modeled using Woschni's correlation [10].

Changes in the potential and kinetic energy of the control volume are neglected. The working fluid is assumed to be an ideal gas of unchanging composition:

$$PV = mRT \tag{3}$$

P is the pressure in the control volume
V is the volume of the control volume, taken to be the crank angle-dependent cylinder volume
m is the mass in the control volume
R is the specific gas constant for the working fluid
T is the temperature of the working fluid

Continuity of mass also applies to the control volume:

$$dm = \dot{m}_i - \dot{m}_e \tag{4}$$

dm is the mass differential in the control volume

Equations 2-4 are used to derive equations for the differential cylinder pressure and the differential temperature:

$$dP = \frac{(\gamma-1)dQ - \gamma P dV + PV\frac{d\gamma}{\gamma-1} + (\gamma-1)(\dot{m}_i h_i - \dot{m}_e h_e)}{V} \tag{5}$$

$$dT = \frac{PdV+VdP}{mR} - T\frac{dm}{m} \tag{6}$$

dV is the differential volume of the control volume

γ is the ratio of specific heats, which is assumed to be a function of temperature only [15]:

$$\gamma = 1.35 - 6\cdot 10^{-5}T + 1\cdot 10^{-8}T^2 \tag{7}$$

The gas exchange is simulated by computing the mass flow rates through the valves for the cases of choked and non-choked flow [10]:

$$\dot{m} = \frac{C_D A_R P_{hi}}{\sqrt{RT_0}}\sqrt{\gamma}\left(\frac{2}{\gamma+1}\right)^{(\gamma+1)/2(\gamma-1)} \text{ if } \frac{P_{low}}{P_{hi}} \le \left(\frac{2}{\gamma-1}\right)^{\gamma/\gamma-1} \tag{8}$$

$$\dot{m} = \frac{C_D A_R P_{hi}}{\sqrt{RT_0}}\left(\frac{P_{low}}{P_{hi}}\right)^{1/\gamma}\sqrt{\frac{2\gamma}{\gamma-1}\left[1-\left(\frac{P_{low}}{P_{hi}}\right)^{\gamma-1/\gamma}\right]} \tag{9}$$

C_D is the experimentally measured discharge coefficient, which depends on the valve lift. Valve lift curves have also been measured experimentally and are used to calculate C_D for each crank angle.
P_{hi} is the greater of the cylinder pressure or the measured static pressure in the exhaust/intake.
P_{low} is the lesser of the cylinder pressure or the measured static pressure in the exhaust/intake.
T_0 is the temperature of the medium flowing through the valves in question, be it intake charge, cylinder contents, or hot exhaust gases
A_R is taken to be twice the valve curtain area (since there are two of each kind of valve):

$$A_R = 2\pi D_v L_v \tag{10}$$

D_v is a characteristic valve diameter
L_v is the experimentally measured valve lift

Equations 4, 5, and 6 are evaluated and integrated using a fourth-order Runge-Kutta method and a step size of 0.25 CAD; the results are insensitive to changes in step size at this resolution. A motored pressure trace ($dQ = 0$) is also integrated for use with the Woschni heat transfer correlation. Initial and boundary conditions are taken from test bench data. Wall temperature is estimated to be 150 °C based on the piston surface temperature measurements shown by Kashdan and Bruneaux for a skip-fired small-bore Diesel engine (scaled to account for the higher engine speed in this work) [16]. The resulting cylinder pressure trace represents one full engine cycle; it is processed using the combustion noise calculation routine described above. In this way, a value of combustion noise can be computed for any arbitrary heat release profile.

For the initial simulations, heat release profiles are derived from the measured results as follows: the pilot and main heat release events are observed to occur with a significant temporal separation for a dwell of 1200 µs. The sharp, narrow heat release profile that is characteristic of the pilot combustion is taken and the negative excursions and waviness surrounding it are removed. The main heat release profile is taken and simplified in a similar manner. Finally, these two basis heat release profiles are added to one another with a variable delay and phasing.

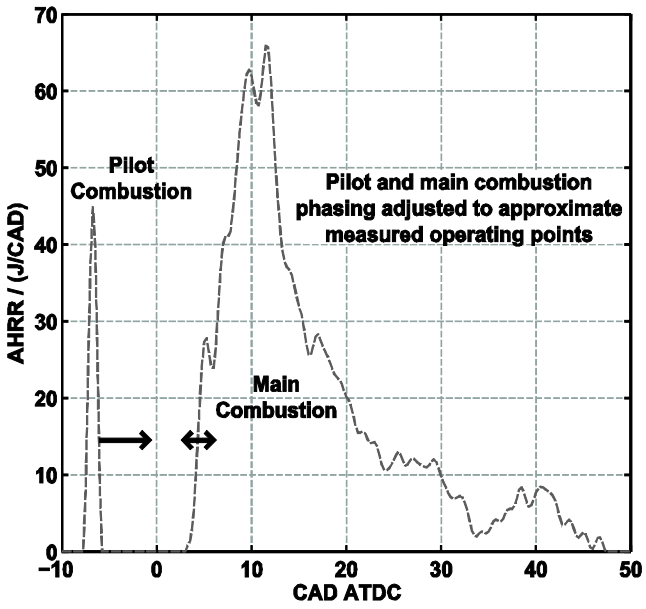

Figure 3: Independent pilot and main heat release events as inputs for initial simulations

The starts of the heat release events are adjusted to mimic the measured starts of combustion for each dwell, and the simulation is run for each dwell. Phasing of the main heat release event changes much less than the phasing of the pilot heat release. Further simulations are performed with different heat release profiles; these profiles will be described as the results are presented and discussed.

Results

Measured trends

As described above, initial investigations are performed with the metal piston top and with fired operation. Dwell is varied from 80 µs to 1200 µs, and a single injection serves as a reference. The pilot and main injections are block shifted to maintain the MFB50 given in Table 2 (with a tolerance of ±0.5 CAD). Because the injector solenoid current is measured both in fired engine operation and with the HDA, the measured injection rates can be synchronized with the measurements taken in the engine (engine speed is assumed to remain constant throughout the portion of the cycle during which the injection occurs). Start of injection (SOI) is computed from the rate of injection data as the last positively sloped zero crossing before an injection event. SOI is shown in Figure 4 for the pilot (SOI_{pilot}) and main (SOI_{main}) injections as a function of dwell.

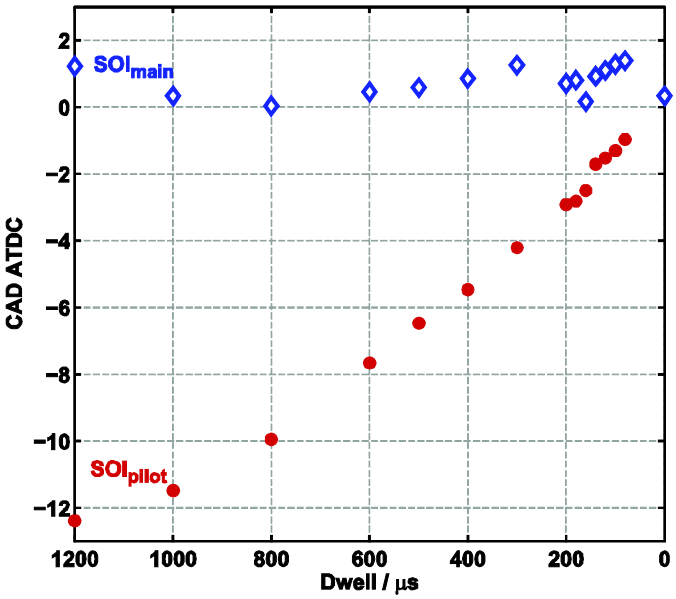

Figure 4: Start of injection (SOI) for pilot and main injections as a function of dwell

The trend in combustion noise is shown in Figure 5 as a function of dwell; the error bars represent two standard deviations (computed or 50 cycles) in each direction. Experiments have also been performed with a second, nominally identical injector, and the results (not shown) are closely repeatable. Standard deviations of combustion noise for a given dwell are typically less than 0.4 dB(A). Although the highest standard deviations typically occur for dwells of less than 200 µs, they are often comparable to the standard deviation for a single injection. The single injection case is shown in this work as a dwell of zero.

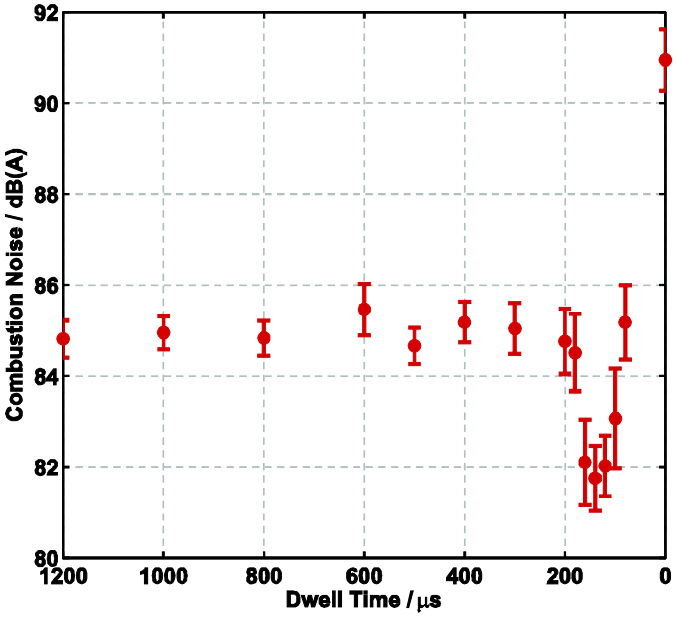

Figure 5: Combustion noise vs. dwell for the pilot-main injection strategy with 2-σ error bars (single injection shown as zero dwell)

The use of a pilot injection significantly decreases noise levels below the level obtained with a single injection: for dwells longer than 200 µs this reduction is approximately 6 dB. However, a further decrease in combustion noise is observed as the dwell decreases below 200 µs, and the minimum occurs at a dwell of 140 µs. The minimum noise levels are approximately 3 dB below the levels obtained with longer dwells; 3 dB corresponds to a factor of two in terms of acoustic power. Understanding the causes of this noise minimum is the goal of this research project. For dwells shorter than 140 µs, combustion noise levels again increase, and for a dwell of 80 µs, combustion noise levels are close to the 85 dB(A) level that is measured for longer dwells. The coefficient of variance (COV) of $IMEP_g$ is typically highest at dwells near 140 µs, but COV remains below 2.5% for all dwells tested. Normalized indicated specific exhaust emissions and filter smoke numbers for these tests are shown in Figure 6; they have been normalized by the levels measured for the single injection case and shown at a dwell of zero.

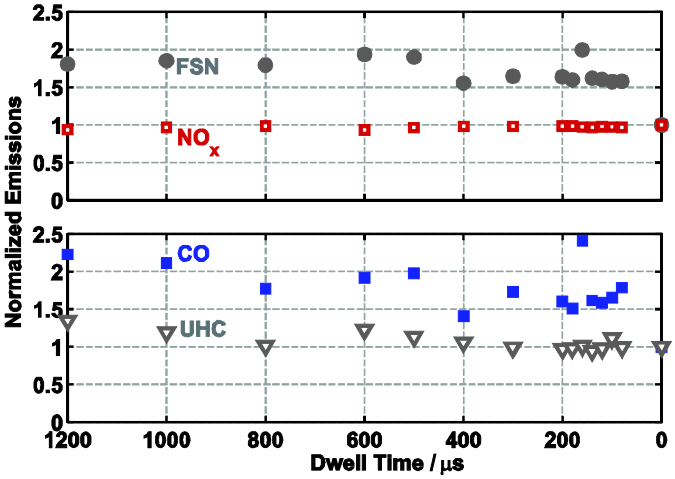

Figure 6: Specific exhaust emission levels (computed in g/kgf) normalized by the single injection (dwell = 0) values: FSN, NO_x, CO, and UHC vs. dwell

For this operating point, NO_x emissions are highest with a single injection, but only slightly lower with a pilot injection. They do not change significantly as dwell changes. FSN levels are higher with a pilot injection than without. Local maxima in FSN occur at dwells of 600 µs and 160 µs. The behavior in FSN at dwells less than 200 µs is not always repeatable: local maxima appear at different dwells and their magnitudes vary from test to test, but local maxima in FSN values are never observed for a dwell of 140 µs. Higher FSN levels are typically associated with higher CO levels, which suggests that the rich mixtures responsible for the formation of soot may also be responsible for the formation of excess CO at shorter dwells. Unburned hydrocarbon (UHC) levels are generally low; they correspond to approximately 0.1% of the injected fuel mass. For shorter dwells, UHC levels are most similar to those obtained with a single injection. Note that the noise minimum seen in Figure 5 at a dwell of 140 µs occurs without penalties in pollutant emissions (when compared to other dwells).

Injection rate, rate shaping, and heat release data

Rates of injection are shown for several dwells and for the single injection in Figure 7. These are phased so that the main injection occurs at zero for each case (the actual starts of main injection are shown in Figure 4). Emphasis is placed on the behavior during the initial phase of the main injection event.

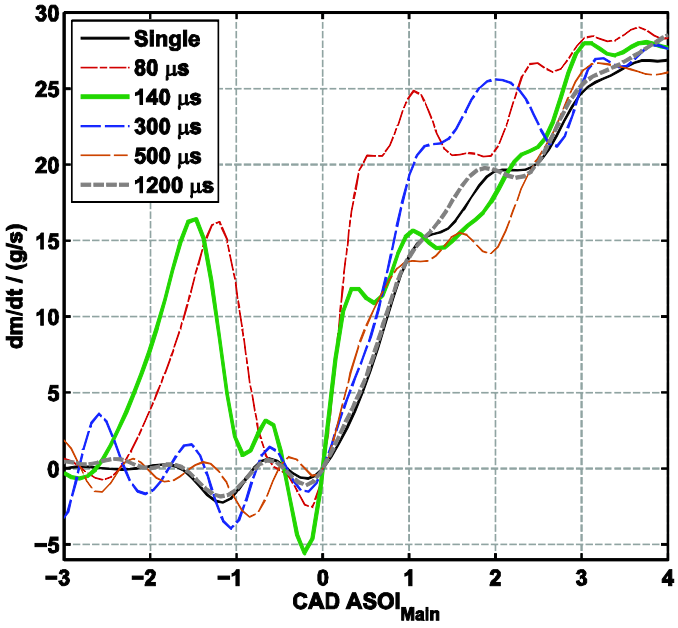

Figure 7: Rates of injection for several dwells and the single injection case, phased according to the start of the main injection (SOI_{Main})

The pilot injection rate takes on a highly repeatable form for all dwells tested (the pilot injection for dwells longer than 140 µs cannot be seen in Figure 7). Differences in injection rate profiles between the different dwells become apparent during the initial rise of the main injection. The change in shape of this initial rise is often referred to as "rate shaping". At a dwell of 80 µs, the main injection rise rate is the highest of all dwells tested. After the initial rise is finished (at approximately 3 CAD $ASOI_{Main}$ in Figure 7), the main injection rate traces behave similarly. The maximum injection rate does not depend on dwell in any systematic way, and the differences in quasi-steady injection rates between the various dwells are typically insignificant.

Calculated heat release rate data and measured rates of injection are used to compute ignition delay for each dwell. In this work, ignition delay is defined as the duration in crank angle degrees between the measured start of pilot injection and the start of combustion (the first positive-sloped zero crossing of the AHRR associated with the beginning of measurable pilot heat release). Ignition delay is plotted against dwell in Figure 8.

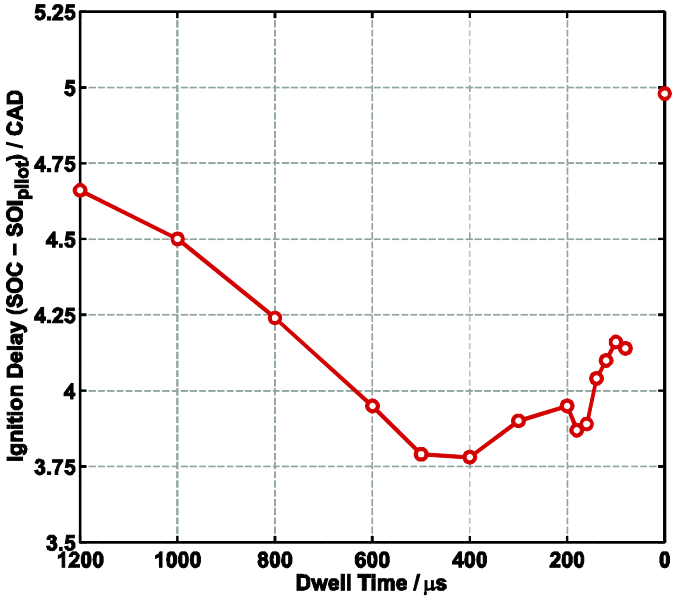

Figure 8: Ignition delay vs. dwell for the pilot-main injection strategy (zero dwell refers to the single injection case)

The ignition delay obtained with a single injection is longer than the ignition delay obtained with a pilot injection regardless of dwell. The pilot injection timing is dictated by the dwell, the pilot injection energizing time, and the location of MFB50 (13 CAD ATDC). As dwell increases beyond 400 µs, the pilot fuel is injected earlier and into an increasingly cooler environment, so the ignition delay increases. For dwells shorter than 400 µs, the ignition delay begins to increase until a dwell of 200 µs. It then decreases slightly for a dwell of 180 µs, but increases as dwell decreases further. Decreasing the FIR filter cutoff frequency results in shorter computed ignition delays and nearly removes this slight decrease, but amplifies the trend of increasing ignition delays for dwells shorter than 180 µs. This increase in ignition delay at short dwells appears to be a real effect and not an artifact of cylinder pressure filtering. It may be the result of an interaction between the main injection and the pilot mixture field; this interaction is discussed in more detail later.

Liquid penetration is computed from the imaging data as described in the appendix for each of 45 cycles. The temporal development of the liquid length measured at one jet is shown in Figure 9 for each cycle, as is the ensemble-averaged liquid length. Aside from an anomaly at the beginning of the pilot injection that is related to limitations of the background subtraction routine, the liquid penetration behaves nearly linearly for the rise rate of both injection events. This rise rate behavior is highly repeatable for both injections for all cases tested, and suggests that the fuel jet dynamics are governed primarily by the liquid fuel at this early stage.

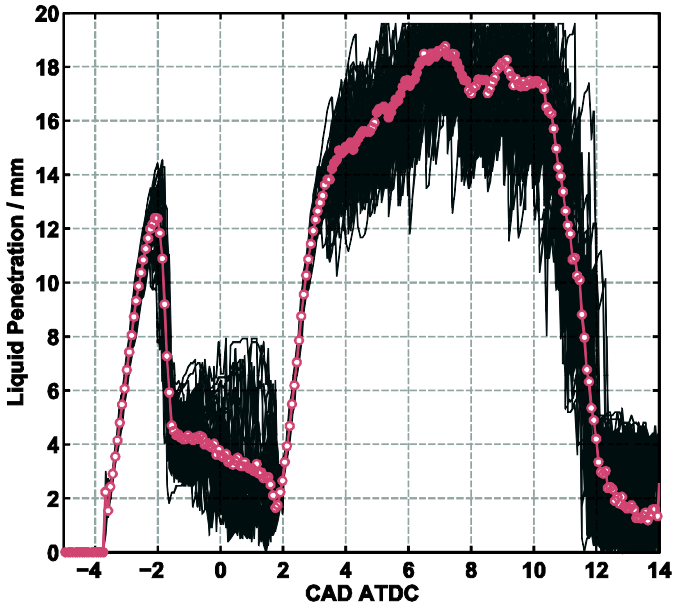

Figure 9: Liquid penetration for individual cycles (black) and ensemble averaged (line with circle markers) for a dwell of 300 µs

The initial linear liquid penetration is consistent with the short-time behavior of a diesel jet as described in [17] and measured by others, for example in [18] and [19]. The initial liquid penetration rate of the pilot injection is comparable to the data shown in [20] for a similar ambient density, rail pressure, and nozzle hole size. For some cycles, the penetration of liquid fuel extends past the edge of the image and into the outer region of the bowl where it cannot be seen. This is evidenced in Figure 9 by clipping of the individual cycles. As a result, the liquid penetration is not accurate for crank angles between approximately 5 and 11 CAD ATDC.

The computed liquid penetration for crank angles between the pilot and main injections fluctuates from cycle to cycle. This is due to liquid fuel that either dribbles from the injector or that remains near the injector, but for some jets it is related to limitations of the background subtraction routine. Data measured after the pilot injection has finished and before the main injection has started is omitted from the following figures. The liquid jet penetration behavior is not the same for every jet; some are characterized by shorter pilot injection liquid lengths. These differences typically become smaller during the main injection. One such jet is chosen for comparison between the various dwells, but the general trends observed in liquid penetration are similar for other jets, particularly during the main injection rise rate. The ensemble-averaged liquid lengths are compared in Figure 10 for each dwell tested and for the single injection. As was the case with the measured rates of injection, emphasis is placed on the initial rise of the main injection.

The liquid length behavior for the pilot injection does not appear to change as dwell is varied. The end of the pilot injection is characterized by a contraction in liquid length, and for the dwell of 300 µs, the measured liquid lengths become noisy and erratic during the hydraulic dwell. This behavior is attributed to the background subtraction routine, as no liquid fuel is clearly observed in this region of the image at this time. As the main injection starts, the liquid length again increases, and the penetration rates appear to be different for each dwell. After the initial rise, the liquid penetration behaves similarly for all of the dwells.

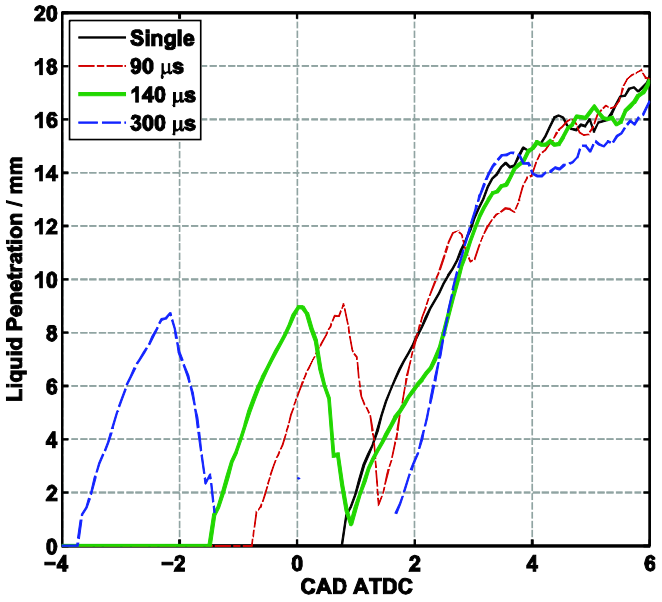

Figure 10: Liquid penetration comparison for a single jet with dwell as a parameter

In order to characterize the differences in the liquid length behavior during the first phase of the main injection, the time derivative of the liquid length curves is calculated and averaged over all seven jets. The resulting penetration rate curves are shown at the bottom of Figure 11. The measured rates of injection are shown at the top of Figure 11). Note that the rate of injection is shown for a dwell of 80 µs, whereas the jet penetration rate is shown for a dwell of 90 µs; injection rate measurements suggest that the differences in rate shapes between these two dwells are minimal. Only positive penetration rate values are shown in Figure 11.

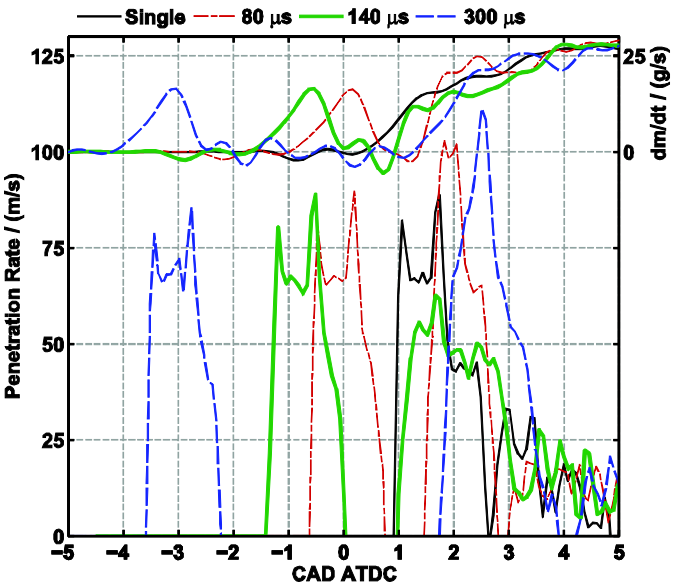

Figure 11: Optically measured liquid penetration rate (bottom) and rate of injection as measured by the HDA (top) with dwell as a parameter

The shape of the optically measured jet penetration rate curves for the pilot injection events are very similar to one another and to that of the initial phase of the single injection. The phasing of the pilot injection jet penetration rates (bottom of Figure 11) relative to their corresponding injection rate profiles (top of Figure 11) is consistent for each dwell. As indicated by Figure 4, the single injection begins at an earlier crank angle than the main injection for dwells of 80 µs, 140 µs, and 300 µs. Also, the main injection for a dwell of 140 µs starts before the main injection for dwells of 80 µs and 300 µs. This behavior is also observed in the jet penetration rate data (bottom of Figure 11). However, the jet penetration rate data (bottom of Figure 11) indicate that the main injection for a dwell of 90 µs begins at an earlier crank angle than for a dwell of 300 µs. This is a slight deviation from the trend shown in the HDA data (top of Figure 11), which is an indication of the uncertainty involved in such comparisons. The peak main injection jet penetration rates (bottom of Figure 11) for a dwell of 140 µs are lower than for any other case; this behavior is consistent with the lower rates of injection (top of Figure 11) for this dwell. The phasing and amplitudes of the maxima in the penetration rates agree qualitatively with the corresponding trends in the injection rate data.

The comparison shown in Figure 11 provides strong evidence that injection rate shaping of the first phase of the main injection is occurring, and that this rate shaping changes as dwell changes. The qualitative agreement between the HDA data (top of Figure 11) and the optical jet penetration rate data (bottom of Figure 11) lends credibility to the rates of injection measured outside the engine with the HDA for these highly dynamic injection schedules.

Direct comparison between the measured injection rate, the AHRR, and the computed combustion noise values (from Figure 5) provides evidence that although rate shaping of the main injection is likely occurring in the engine, the trends in rate shaping do not correspond to the trend in combustion noise. The first comparison is shown in Figure 12.

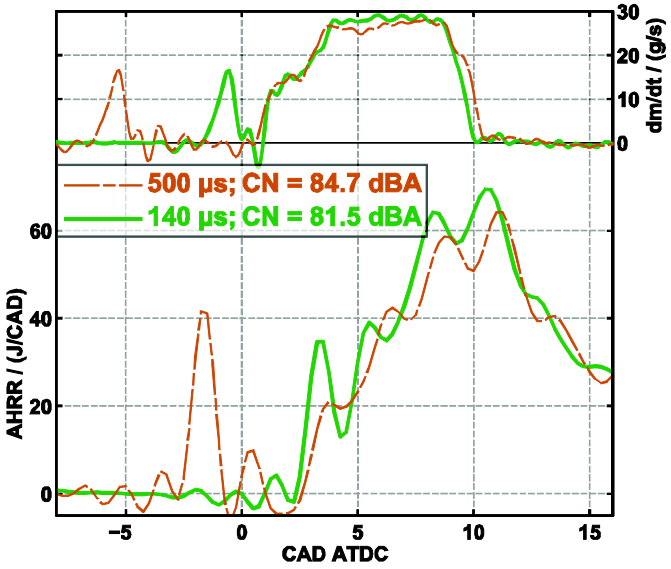

Figure 12: Rates of injection, combustion noise values, and AHRR for dwells of 500 µs and 140 µs

The shapes of the main injection events are similar for these two dwells, but the combustion noise is significantly louder for the 500 µs dwell. Relatively small differences in the main portions of the AHRR traces do not correlate with this significant difference in combustion noise. The main injection is already underway at the time of pilot

heat release, and the initial peak in AHRR attributed to the combustion of the pilot injection is lower at a dwell of 140 µs than at a dwell of 500 µs. This effect is demonstrated for more dwells in Figure 13. For dwells shorter than 300 µs, the peak pilot AHRR decreases. Peak pilot AHRR values reach their minimum at a dwell of 140 µs. They are not shown in Figure 13, but peak pilot AHRR values increase for dwells shorter than 140 µs.

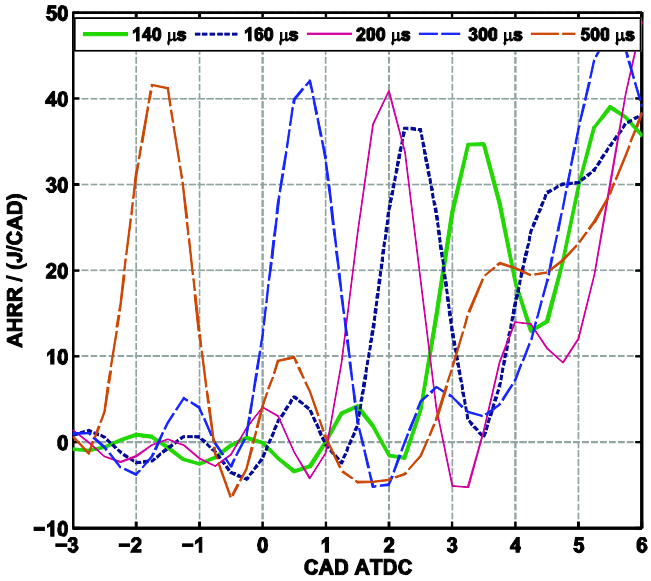

Figure 13: Pilot AHRR suppression for close-coupled pilot injections; dwells of 140 µs, 160 µs, 200 µs, 300 µs, 500 µs

A second comparison between injection rate, combustion noise, and AHRR is shown in Figure 14 for dwells of 80 µs and 1200 µs. The start of the main injection occurs at very nearly the same crank angle for these two dwells. The shapes of the main injection rates, however, are different: the highest measured main injection rise rate occurs at a dwell of 80 µs, whereas the rise rate for a dwell of 1200 µs is closer to that of a single injection (see Figure 7). Despite these differences in main injection rate shape, the difference in combustion noise levels is only 0.4 dB.

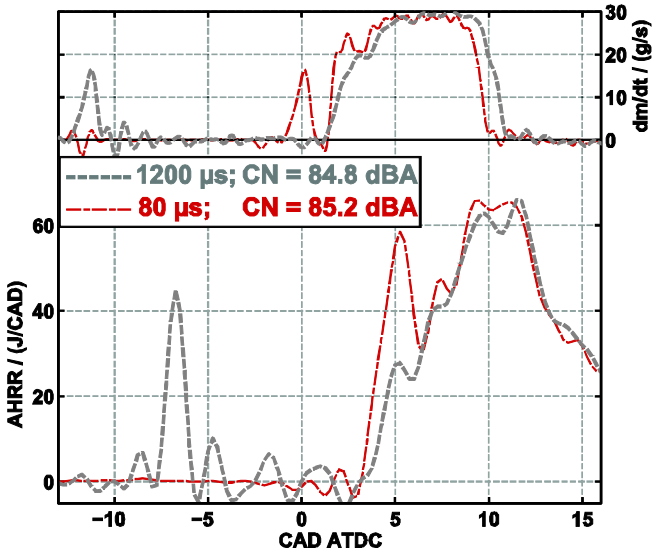

Figure 14: Rates of injection, combustion noise values, and AHRR for dwells of 1200 µs and 80 µs

The AHRR traces for these two dwells are quite different. At a dwell of 80 µs, the initial heat release peak is higher than what could be attributed to the pilot injection alone. As was the case with a dwell of 140 µs, the main injection starts before any significant heat release is observed.

The data shown in Figure 12 and Figure 14 suggest that for these conditions, the amplitude of the initial heat release peak is not the dominant factor in determining combustion noise. The reduction in combustion noise for dwells near 140 µs cannot be attributed to the effects of main injection rate shaping, either. A better understanding of the causes of this reduction in noise requires further analysis.

Spectral analysis

Spectral analysis of the cylinder pressure data provide insight about the contribution of each frequency component to combustion noise and how these contributions may differ between different dwells. Sound pressure levels are shown in Figure 15 for dwells of 80 µs, 140 µs, and 300 µs, as well as for the single injection reference case. These sound pressure levels have been computed from measured cylinder pressure traces. Sound pressure levels at frequencies higher than 5 kHz are nearly identical for each of the dwells and are not shown.

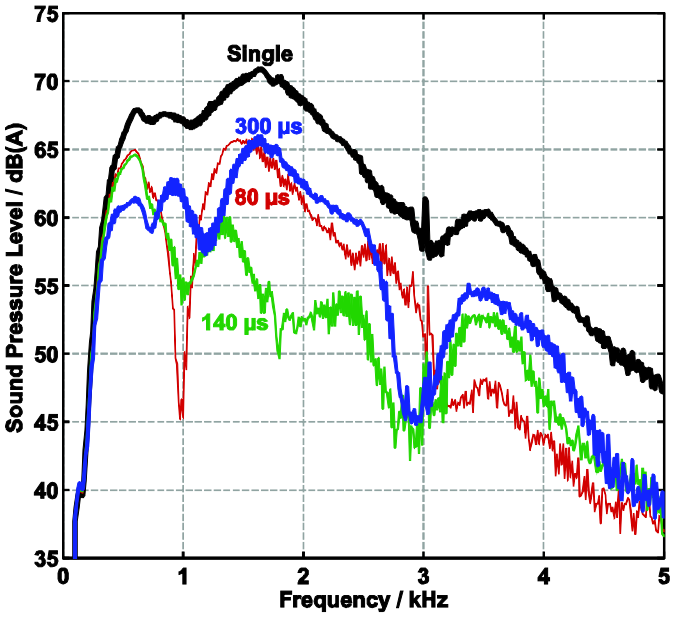

Figure 15: Sound pressure levels for dwells of 80 µs, 140 µs, and 300 µs and for a single injection

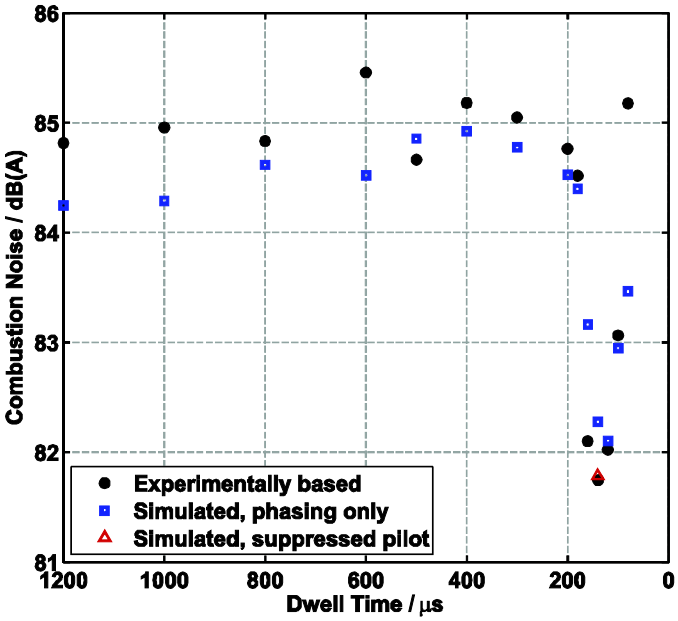

Figure 16: Experimentally based (black dots) and simulated combustion noise levels for a dwell sweep

For frequencies greater than approximately 500 Hz, measured sound pressure levels for the single injection case are higher than for any pilot-main case. The addition of a far pilot (for instance with a dwell of 300 µs) strongly attenuates sound pressure levels over this frequency range, which results in the 6 dB decrease in combustion noise observed in Figure 5. As dwell decreases from 1200 µs to approximately 200 µs, the shapes of the sound pressure spectra change, but decreases in certain frequency ranges are effectively balanced by increases in other frequency ranges, so the net contribution to combustion noise is very small. This is reflected in the flat trend in measured combustion noise values (Figure 5) for longer dwells. At the noise-minimum dwell of 140 µs, a specific frequency range can be identified that is responsible for the combustion noise minimum. As seen in Figure 15, the sound pressure level for a dwell of 140 µs is significantly lower than both the 80 µs and 300 µs dwell cases in the frequency range between approximately 1.3 kHz and 2.8 kHz. Other dwells have sound pressure levels that may be close to the sound pressure levels at a dwell of 140 µs in this frequency range, but this only holds true for some small portion of the range. Attenuated amplitudes of the cylinder pressure frequency components with frequencies in this range are responsible for the combustion noise minimum that occurs at a dwell of 140 µs.

Zero-dimensional simulation results

Zero dimensional modeling provides insight into the factors responsible for the trend in combustion noise. The pilot and main heat release profiles shown in Figure 3 were phased to match the AHRR traces that were calculated from the measured cylinder pressure data at each dwell. These simulated heat release rate profiles are used as inputs for the zero-dimensional simulation. The effects of main injection rate shaping are neglected entirely, as the main combustion heat release profile does not change shape as dwell changes. For each simulated dwell, a cylinder pressure trace and a corresponding combustion noise is computed. The combustion noise results of the simulations are compared with the experimentally based combustion noise data in Figure 16.

The initial simulation results are shown as blue squares, and the decrease in combustion noise for dwells shorter than 200 µs is reproduced well. The measured minimum combustion noise is lower than the minimum simulated noise value for this initial phasing variation. To simulate the effects of pilot AHRR suppression (visible in Figure 13), the model pilot heat release rate trace was scaled by 90% for the simulated dwell of 140 µs to mimic the measured data. The resulting simulated combustion noise is shown in Figure 16 with a red triangle; it is very close to the measured minimum in combustion noise. The combination of changing the heat release phasing and decreasing the pilot heat release rates to mimic the measured data can reproduce the measured trend in combustion noise very well. Combustion noise is not always accurately predicted at longer dwells, but the purpose of this simulation is not model validation. Rather, it is to capture the combustion noise reduction mechanism in a simple model so it can be understood.

The sound pressure levels computed from the measured data (shown in Figure 15) indicate that for a dwell of 140 µs, the sound pressure level is attenuated in a specific frequency range. The impact of pilot suppression (shown in Figure 16) on sound pressure level is difficult to measure, but sound pressure levels can be calculated for the two simulated cylinder pressure traces: the 140 µs dwell case and the 140 µs dwell case with the attenuated pilot heat release trace. These two sound pressure level spectra are shown in Figure 17. The decrease in noise by pilot AHRR suppression is attributed to broadband attenuation of frequency components in the frequency range from approximately 1 kHz to 5 kHz.

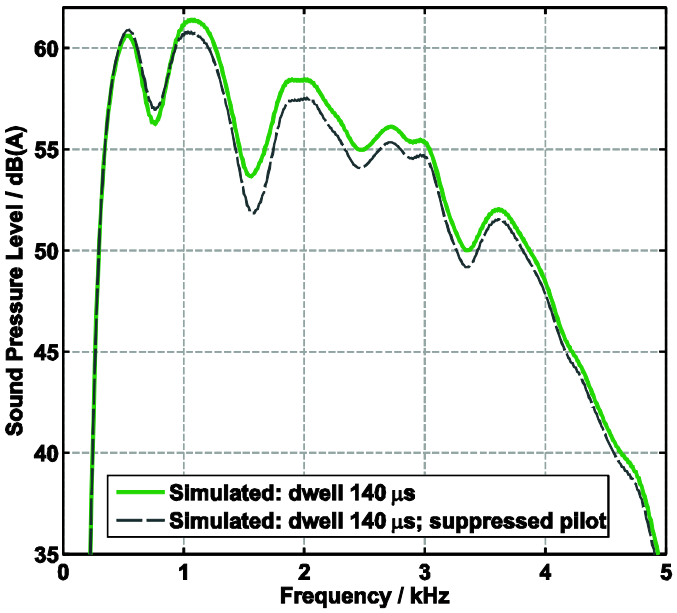

Figure 17: Simulated sound pressure levels for a dwell of 140 µs, with and without simulated suppression of the pilot heat release

The shape of the simulated main heat release rate is complex, and the main heat release phasing changes slightly as dwell is varied. The influence of the shape and phasing of the main heat release on combustion noise is investigated with highly simplified heat release profiles and a fixed start of main heat release; these are shown in Figure 18. The total heat released for each heat release event (the areas under the pilot and main heat release rate traces) is the same as for the traces shown in Figure 3. For this set of simulations the start of pilot combustion (SOC_{pilot}) is varied. The trend of combustion noise vs. SOC_{pilot} is shown in Figure 19.

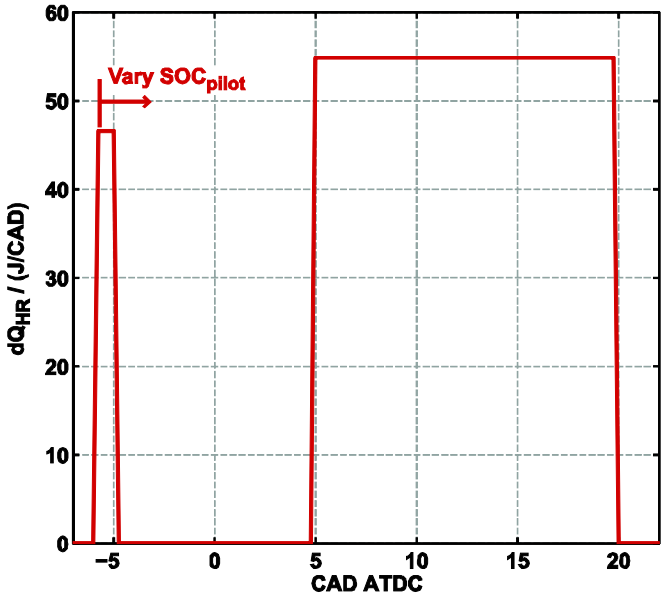

Figure 18: Simulated top hat heat release profiles for zero-dimensional thermodynamic simulations

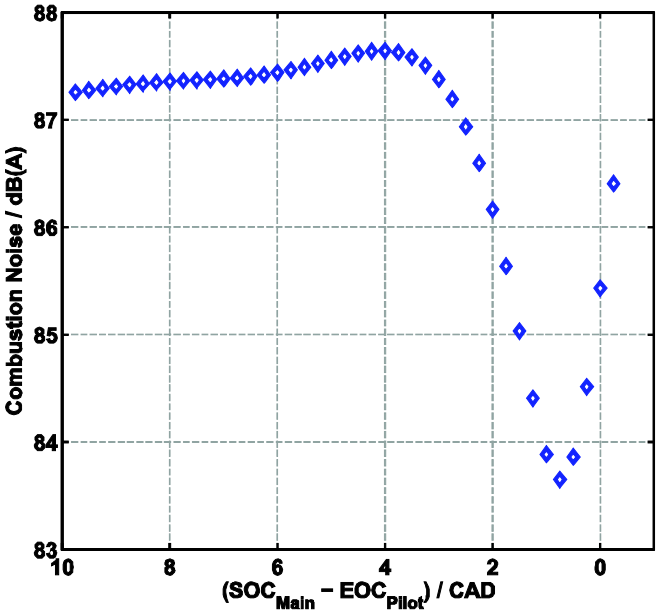

Figure 19: Simulated combustion noise levels with top hat heat release profiles for a sweep of SOC_{pilot}

The trend in combustion noise with changing SOC_{pilot} is remarkably similar to the one obtained with more realistic heat release rate profiles (cf. Figure 16). Even with these highly simplified heat release profiles, a minimum in combustion noise occurs as the delay between heat release events decreases. Combustion noise reaches its minimum just before the two top hat heat release rates begin to overlap. Inspection of the heat release profiles used for the first simulations (shown in Figure 3) indicates that the minimum in combustion noise for decreasing dwells occurs just after the heat release rates begin to overlap. As the degree of overlap of the heat release profiles then increases, the combustion noise increases.

Band pass filtering of measured cylinder pressures

The simulation results demonstrate the importance of the relative phasing of the pilot and main heat release events in determining combustion noise, but the mechanism by which combustion noise is decreased is still unclear. On the other hand, the measured sound pressure level spectra shown in Figure 15 demonstrate that changing the dwell alters the frequency content of the cylinder pressure trace in a specific frequency range (~1.3 kHz – 2.8 kHz). Further analyses are performed in time space using band pass filters to examine features of the measured cylinder pressure traces. Differences in sound pressure levels between the 300 µs and 80 µs cases become much larger at frequencies higher than 2.6 kHz (see Figure 15), so a band pass filter was applied to ensemble-averaged pressure traces with a pass band between 1.3 kHz and 2.6 kHz. The ensemble-averaged measured traces, as well as the band pass filtered traces, are shown in Figure 20. The filtered traces have been shifted vertically to facilitate

comparison with the unfiltered traces.

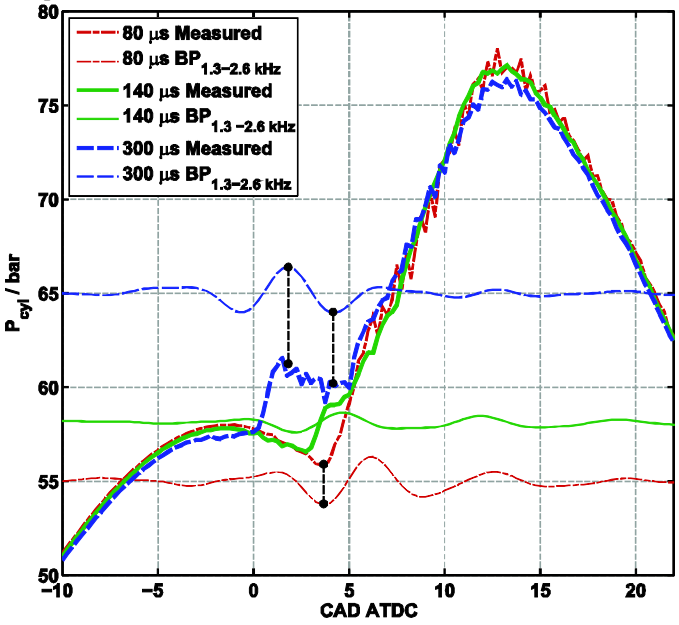

Figure 20: Ensemble-averaged cylinder pressure traces and band pass (BP) filtered cylinder pressure traces for dwells of 80 µs, 140 µs, and 300 µs. Filter pass band: 1.3 - 2.6 kHz.

The filtered pressure signals are nearly identical for the majority of the cycle, but exhibit significant differences at crank angles near TDC. For a dwell of 300 µs, the most prominent peak and trough in the filtered signal correspond closely to the pressure peak associated with the pilot combustion and the trough that results from cooling and expansion before the main combustion, respectively. At a dwell of 80 µs, the trough of the filtered pressure trace coincides with the unfiltered pressure trough that results from the pressure decrease after TDC and the combustion that begins near 4 CAD ATDC. The increase in the filtered pressure trace after the most prominent trough coincides with the increase in pressure due to the combustion of the main injection.

For a dwell of 140 µs (that which gives the minimum combustion noise), a decrease in unfiltered pressure is also observed after TDC, but it is smaller than the one observed for a dwell of 80 µs. The pressure increases due to the combustion of the pilot, but does not decrease before the heat released by the main injection fuel begins to increase the pressure further. The most prominent trough in the filtered pressure trace does not directly coincide with the unfiltered pressure trough, and the most prominent filtered pressure peak does not correspond to an unfiltered peak.

The band pass filtered pressure traces seen in Figure 20 are compared directly in Figure 21. Amplitudes of the filtered pressure oscillations are highest for dwells of 80 µs and 300 µs; this agrees with the spectral data shown in Figure 15.

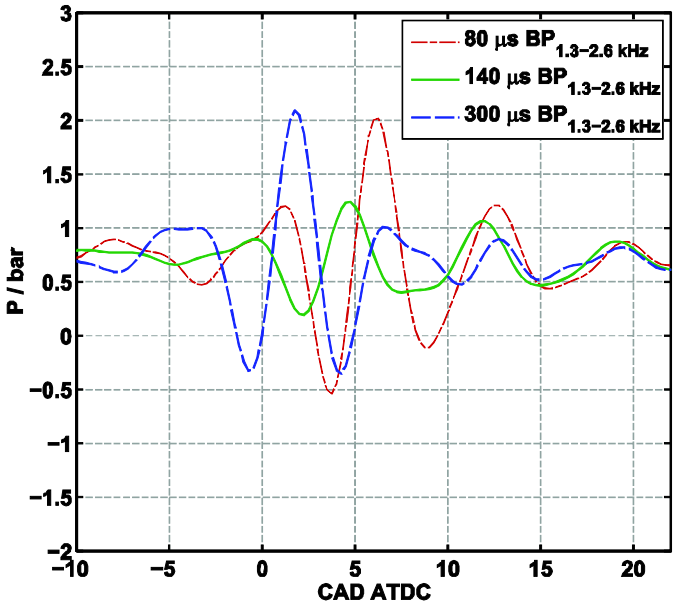

Figure 21: Direct comparison of band pass (BP) filtered cylinder pressure traces for dwells of 80 µs, 140 µs, and 300 µs. Filter pass band: 1.3 - 2.6 kHz.

Discussion

The experimental results provide evidence that the mechanism responsible for the combustion noise trend (shown in Figure 5) does not depend on rate shaping of the main injection. Rather, analyses of experimental data and zero-dimensional simulation results suggest that the combination of the following factors is responsible for the observed combustion noise behavior as dwell changes:

1. The changing phasing of the pilot heat release event relative to the main heat release event
2. Suppression of the pilot AHRR by the main injection

The first factor is likely responsible for the general shape of the combustion noise trend, whereas the second mechanism may act to decrease noise levels further in regimes with temporal overlap between pilot combustion and main injection. Furthermore, it has been shown that frequency components of cylinder pressure in the critical range between approximately 1.3 kHz and 2.8 kHz are responsible for the minimum in measured combustion noise at dwell times near 140 µs (see Figure 15). For an engine speed of 1500 rpm, these frequencies correspond to periods of approximately 3.5 to 7 CAD. In other words, cylinder pressure oscillations in this frequency range have periods on the order of 3.5 to 7 CAD. This is confirmed by the filtered pressure traces shown in Figure 21. The accumulated effect of frequency components in this frequency range is significant at crank angles near the starts of the pilot and main heat release events (this is evident in Figure 20).

The lowest natural frequency of the cylinder occurs between 4 and 5 kHz, which suggests that the combustion noise trend in question is not acoustic in nature. This is supported by the fact that the noise trend can be reproduced with a relatively simple zero-dimensional model that wholly neglects acoustical phenomena. The mechanism by which changing the time between the pilot and main heat release events (the first factor listed above) impacts combustion noise is not yet understood.

We have identified two potential mechanisms that will be proposed here but investigated more thoroughly in the future. The first mechanism involves the interaction between pressure increases due to heat release and pressure decreases due to downward piston motion and heat loss. The frequency content associated with the compression and expansion of the cylinder contents due to piston motion is rather small in magnitude, but the combination with two combustion events changes this. The data shown in Figure 20 suggest that for combustion events phased shortly after TDC, the pressure oscillations at dwells shorter and longer than the noise optimized dwell of 140 μs tend to have significant components with oscillation periods of between 3.5 and 7 CAD. The peaks and troughs of the band pass filtered pressure traces correspond to peaks and troughs in the unfiltered traces. This mechanism implies that the noise behavior is strongly coupled to combustion phasing. For instance, if the starts of the pilot and main combustion events both occurred before TDC, pressure decreases due to expansion of the cylinder contents would not occur, and pressure oscillations in the 1.3 to 2.8 kHz range would be fundamentally altered. This potential mechanism will be investigated further using the simulation tools developed in this work.

The second potential mechanism by which the changing time between the pilot and main heat release events may create the observed trend in combustion noise is motivated by the data shown in Figure 21. Apparent reflection symmetry exists between the filtered pressure traces for dwells of 80 and 300 μs (this is most noticeable in the crank angle range between -3 CAD ATDC and 11 CAD ATDC). The dwell of 140 μs falls in between these two dwells, and the amplitude of the band pass filtered pressure trace shown in Figure 21 also exhibits some degree of reflection symmetry (centered around 3 CAD ATDC). These observed symmetries may indicate that as dwell and heat release phasing change, contributions to the pressure oscillations resulting from the pilot and main heat release events may pass through a region of destructive interference for frequencies in this critical range. This interference could explain the increase of combustion noise on either side of the noise minimum. An important difference between this mechanism and the first one is that this mechanism would be largely independent of the overall combustion phasing and sensitive to dwell. Initial analyses suggest that this second mechanism is indeed significant, and future work will focus on understanding and describing the mechanism.

Suppression of the apparent pilot heat release due to the main injection (the second factor listed above) could conceivably occur via two mechanisms: cylinder charge cooling due to heating and vaporization of fuel injected during the main injection and/or direct interaction of the main injection with the combusting pilot mixture field. This first mechanism would not alter the total amount of energy released by the combusting pilot mixture, but would rather decrease the magnitude of the apparent heat release as fuel heating and vaporization removes sensible enthalpy from the cylinder contents. The energy required to heat and vaporize fuel injected during the main injection can be estimated as follows.

Detailed thermodynamic data are not available for the fuel used in this study, but they are available for n-hexadecane, so thermodynamic properties of n-hexadecane (taken from [21] and [22]) are used for this analysis. They are listed in Table 3.

Table 3: Thermochemical properties of n-Hexadecane

C_p (373.15 K, 5.0 MPa)	2.44 J/(g K)
T_b (boiling point)	560.01 K
h_v (at T_b, 1 atm)	228.9 kJ/kg

Fuel mass is computed by numerical integration of the injection rate curves. For a dwell of 140 μs, the mass of fuel injected between the start of the main injection to either the time of peak pilot heat release or to the local minimum in heat release following the peak pilot heat release (see Figure 12) is either 4.2 mg or 6.3 mg. It is assumed that the amount of fuel being heated and vaporized during the combustion of the pilot injection fuel has a mass that falls within this range. The sensible enthalpy change associated with heating this mass of n-hexadecane to its boiling point is estimated by the following equation:

$$\Delta H_s = mc_p\Delta T \tag{11}$$

m is the mass of fuel (either 4.2 mg or 6.3 mg)

c_p is the specific heat at constant pressure and is assumed not to change with temperature

ΔT is the change in temperature between the fuel's initial temperature (assumed to be 90 °C) and its boiling point

Evaluating Equation 11 for the two masses computed above yields a sensible enthalpy change of between 2.0 and 3.0 J to heat the n-hexadecane from the coolant temperature to its boiling point. This analysis neglects friction heating of the fuel as it flows through the nozzle holes.

For the masses of fuel used in this analysis, the heats of vaporization are between 1.0 and 1.4 J. So the total enthalpy change associated with heating and vaporizing the quantities of n-hexadecane mentioned above is between 3.0 and 4.4 J.

An estimate of the total pilot heat release is computed by numerical integration of the AHRR curve over the crank angle range during which the pilot heat release event occurs. For a dwell of 1200 μs (the longest dwell tested in this work), the total pilot heat release is approximately 47 J, which corresponds to 1.1 mg of fuel being consumed. For a dwell of 140 μs, an estimate of the total pilot heat release is 44 J. The difference between these two quantities is 3 J, which corresponds well with the enthalpy required to heat and vaporize the mass of n-hexadecane injected as part of the main injection during the pilot combustion event. The effect on peak pilot AHRR is strongest at a dwell of 140 μs (see Figure 13 and its description). For dwells longer than 140 μs, the duration of the temporal overlap between the pilot heat release and the main injection decreases. For dwells of 300 μs and longer, the main injection begins after the pilot heat release event has finished, and this suppression mechanism is not active. For dwells shorter than 140 μs, the temporal overlap of the pilot and main heat release events increases the peak AHRR and mitigates this effect. Thus, suppression of the pilot AHRR by the main injection can be attributed to the thermal energy required for heating and vaporization of the main injection fuel.

Measured AHRR data (Figure 14), as well as the zero-dimensional simulation results (Figure 16 and Figure 19) show that the heat release associated with the pilot injection overlaps temporally with

the heat release due to combustion of the main injection. The mechanism for this temporal overlap is not understood. Combustion of the pilot is in progress as the fuel from the main injection is introduced, but it is not known whether combustion of the main mixture field is initiated by auto-ignition reactions or by inflammation as a propagating flame that originates in the burning pilot mixture field. The latter mechanism has been identified in [23] based on CFD simulation results.

Summary

For the close-coupled pilot-main injection strategy employed in this study, changing the energizing dwell between the pilot and main injections affects the combustion noise for a part-load operating point, and a minimum in combustion noise is achieved with a dwell of 140 μs (Figure 5). This minimum is achieved without penalties in pollutant emissions (Figure 6). Changes in dwell alter the shape of the initial rise in injection rate for the main injection (Figure 7). High-speed scattering imaging performed in the engine provides evidence that this rate shaping also occurs in the engine, and it does so in a similar manner to that measured with the injection analyzer (Figure 11). However, the experimental data show that rate shaping of the main injection is not responsible for the observed combustion noise trend (Figure 12 and Figure 14).

Zero-dimensional thermodynamic simulations confirm that the noise reduction mechanism does not depend on changes to the main combustion heat release profile. The combination of two factors is responsible for the trend in combustion noise:

1. The changing phasing of the pilot heat release event relative to the main heat release event
2. Suppression of the pilot AHRR by the main injection

The second factor can be explained by the energy required to heat and vaporize the fuel injected during beginning of the main injection. This energy comes at the expense of sensible enthalpy of the hot in-cylinder gases, and the impact of the pilot heat release on cylinder pressure is reduced. This reduction leads to broadband attenuation of sound pressure levels over a wide frequency range (Figure 17), thereby acting to decrease combustion noise for dwells shorter than approximately 200 μs. While this phenomenon likely occurs within the engine, simulation results suggest that it is only responsible for a small portion of the combustion noise decrease observed at dwells shorter than 200 μs (Figure 16).

The dominant factor impacting the change in combustion noise as dwell varies is the accompanying change in time between the pilot and main heat release events. The mechanism by which this impacts combustion noise is not yet well understood, but we have suggested two possibilities, both of which involve cylinder pressure frequency components in the range of approximately 1.3 to 2.6 kHz. Changes to pressure oscillations in this critical frequency range must be responsible for the noise minimum at a dwell of 140 μs (Figure 15).

The first proposed mechanism suggests that pressure increases due to heat release, as well as pressure decreases due to downward piston motion and heat loss, are responsible for changing the pressure oscillations in the frequency range of 1.3 to 2.6 kHz as dwell changes. At a dwell of 140 μs, the temporal overlap of the pilot and main combustion phases causes a relatively smooth, monotonic pressure rise associated with the combustion. The combustion is phased so that expansion and heat loss do not decrease the cylinder pressure significantly after TDC and before the onset of heat release. In this way, the formation of pressure oscillations in this critical frequency range is impeded. This mechanism implies a strong dependence on overall combustion phasing and will be investigated with future simulation work.

The second proposed mechanism by which the changing phasing of the pilot heat release relative to the main heat release affects combustion noise is that the decrease in noise is caused by destructive interference in the frequency range of 1.3 to 2.6 kHz. This mechanism does not rely on the interaction between the compression and expansion of the cylinder contents or heat loss, but rather on the interaction between the cylinder pressure oscillations caused by the pilot and main heat release events. Although our initial analyses suggest that this mechanism is likely significant, it still needs to be fully understood and characterized.

References

1. Russell, M., Young, C., and Nicol, S.W., "Modulation of Injection Rate to Improve Direct Injection Diesel Engine Noise," SAE Technical Paper 900349, 1990, doi:10.4271/900349.
2. Dürnholz, M., Endres, H., Frisse, P., “Preinjection A Measure to Optimize the Emission Behavior of DI-Diesel Engine,” SAE Technical Paper 940674, 1994, doi:10.4271/940674.
3. The new 1.3 Multijet II 95 HP (Euro5) engine is making its first appearance on the Fiat 500 and 500C. Fiat Group Automobile Press, 25 Nov. 2009. <www.fiatgroupautomobilespress.com/cartelle/zoom/4594>, Available March 2014.
4. Diesel Systems: Common Rail Systems CRS2 with 1,600 to 2,000 bar and solenoid injectors. Robert Bosch GmbH, Diesel Systems, 2011. Available online March 2014.
5. Badami, M., Millo, F., and D'Amato, D., "Experimental Investigation on Soot and NOx Formation in a DI Common Rail Diesel Engine with Pilot Injection," SAE Technical Paper 2001-01-0657, 2001, doi:10.4271/2001-01-0657.
6. Ricaud, J.C. and Lavoisier, F., “Optimizing the multiple injection settings on an HSDI diesel engine,” Proceedings of the Conference on Thermo- and Fluid-Dynamic Processes in Diesel Engines, pp. 251-275, Valencia, 2002.
7. Sahoo, D., Petersen, B., and Miles, P., "Measurement of Equivalence Ratio in a Light-Duty Low Temperature Combustion Diesel Engine by Planar Laser Induced Fluorescence of a Fuel Tracer," SAE Int. J. Engines 4(2):2312-2325, 2011, doi:10.4271/2011-24-0064.
8. Sahoo, D., Miles, P., Trost, J., and Leipertz, A., "The Impact of Fuel Mass, Injection Pressure, Ambient Temperature, and Swirl Ratio on the Mixture Preparation of a Pilot Injection," SAE Int. J. Engines 6(3):1716-1730, 2013, doi:10.4271/2013-24-0061.
9. Miles, P., Sahoo, D., Busch, S., Trost, J. et al., "Pilot Injection Ignition Properties Under Low-Temperature, Dilute In-Cylinder Conditions," SAE Int. J. Engines 6(4):1888-1907, 2013, doi:10.4271/2013-01-2531.
10. Heywood, J.B., *Internal Combustion Engine Fundamentals*, McGraw-Hill, New York: 1988.
11. "The Allrounder." *Moehwald GmbH (Bosch Group) Website*. Moehwald GmbH, n.d. Web. 15 Sept. 2014. <http://www.moehwald.de/runtime/cms.run/doc/English/150/HDA.html>.
12. Busch, S. and Miles, P.C., “Parametric Study of Injection Rates with Solenoid Injectors in an Injection Quantity and

Rate Measuring Device", Proceedings of the ASME 2014 ICEF, October 19-22, 2014 (forthcoming).
13. Colban, W., Miles, P., and Oh, S., "On the Cyclic Variability and Sources of Unburned Hydrocarbon Emissions in Low Temperature Diesel Combustion Systems," SAE Technical Paper 2007-01-1837, 2007, doi:10.4271/2007-01-1837.
14. Shahlari, A., Hocking, C., Kurtz, E., and Ghandhi, J., "Comparison of Compression Ignition Engine Noise Metrics in Low-Temperature Combustion Regimes," SAE Int. J. Engines 6(1):541-552, 2013, doi:10.4271/2013-01-1659.
15. Brunt, M. and Platts, K., "Calculation of Heat Release in Direct Injection Diesel Engines," SAE Technical Paper 1999-01-0187, 1999, doi:10.4271/1999-01-0187.
16. Kashdan, J. and Bruneaux, G., "Laser-Induced Phosphorescence Measurements of Combustion Chamber Surface Temperature on a Single-Cylinder Diesel Engine," SAE Technical Paper 2011-01-2049, 2011, doi:10.4271/2011-01-2049.
17. Naber, J. and Siebers, D., "Effects of Gas Density and Vaporization on Penetration and Dispersion of Diesel Sprays," SAE Technical Paper 960034, 1996, doi:10.4271/960034.
18. Hiroyasu, H. and Arai, M., "Structures of Fuel Sprays in Diesel Engines," SAE Technical Paper 900475, 1990, doi:10.4271/900475.
19. Reitz, R. and Bracco, F., "On the Dependence of Spray Angle and Other Spray Parameters on Nozzle Design and Operating Conditions," SAE Technical Paper 790494, 1979, doi:10.4271/790494.
20. Payri, R., Salvador, F.J., Gimeno, J., de la Morena, J., "Macroscopic Behavior of Diesel Sprays in the Near-Nozzle Field," SAE Int. J. Engines, Vol. 1, Issue 1, 2008; SAE technical paper 2008-01-0929.
21. Lide, D.R. (ed.), *CRC Handbook of Chemistry and Physics*, 84th ed., CRC press, 2003.
22. Banipal, T.S.; Garg, S.K.; Ahluwalia, J.C., "Heat capacities and densities of liquid n-octane, n-nonane, n-decane, and n-hexadecane at temperatures from 318.15 to 373.15 K and at pressures up to 10 MPa," Journal of Chemical Thermodynamics, 1991, 23, 923-931.
23. Hasse, C., Peters, N., "Modelling of ignition mechanisms and pollutant formation in direct-injection Diesel engines with multiple injections," International Journal of Engine Research, Vol. 6, No 3, pp. 231-246, June 1, 2005.
24. Smith, W.J., *Modern Optical Engineering*, 4th ed., McGraw-Hill, New York: 2008.
25. McFarlane, N.J.B., Schofield, C.P., "Segmentation and tracking of piglets in images," Machine Vision and Applications, Vol. 8, Issue 3, pp. 187-193, 1995.

Contact Information

Stephen Busch: sbusch@sandia.gov

Acknowledgments

The authors gratefully acknowledge Chuck Mueller for lending out his high speed camera and Julien Manin for his assistance with the triggering setup for the camera and LED. Magnus Sjöberg and Jeremie Dernotte are acknowledged for their help in reviewing the manuscript and for the useful discussions that ensued.

Support for this work was provided by the United States Department of Energy (Office of Vehicle Technologies) and by General Motors Corporation (agreement FI083070326). This work was performed at the Combustion Research Facility of Sandia National Laboratories in Livermore, California. Sandia National Laboratories is a multi-program laboratory managed and operated by Sandia Corporation, a wholly owned subsidiary of Lockheed Martin Corporation, for the U.S. Department of Energy's National Nuclear Security Administration under contract DE-AC04-94AL85000.

Definitions/Abbreviations

Definitions

$\boldsymbol{A_R}$: reference area for discharge coefficient

$\boldsymbol{C_D}$: dimensionless discharge coefficient

$\boldsymbol{c_P}$: specific heat at constant pressure

$\boldsymbol{c_v}$: specific heat at constant volume

$\boldsymbol{\gamma}$: ratio of c_P to c_v

$\boldsymbol{D_v}$: valve diameter

$\boldsymbol{dQ}$: net heat addition rate

$\boldsymbol{dQ_{HR}}$: heat release rate due to combustion

$\boldsymbol{dQ_{wall}}$: rate of heat loss to walls

$\Delta\boldsymbol{H_s}$: change in sensible enthalpy

$\Delta\boldsymbol{T}$: change in temperature

$\boldsymbol{h_{i/e}}$: specific enthalpy of mass flowing into or out of the cylinder

$\boldsymbol{h_v}$: heat of vaporization

$\boldsymbol{L_v}$: valve lift

$\boldsymbol{m}$: mass

$\boldsymbol{\dot{m}_{i/e}}$: mass flow rate into or out of the cylinder through the valves

$\boldsymbol{P}$: pressure

$\boldsymbol{R}$: specific gas constant for the working medium in the cylinder

$\boldsymbol{T}$: temperature

$\boldsymbol{T_b}$: boiling temperature

$\boldsymbol{U}$: internal energy

$\boldsymbol{V}$: cylinder volume

Abbreviations

AHRR: apparent heat release rate

ASOI: after the start of injection

ATDC: after top dead center

BP: band pass

BTDC: before top dead center

CAD: crank angle degrees

CMOS: complementary metal-oxide semiconductor

EGR: exhaust gas recirculation

ET: energizing time

FIR: finite impulse response

$IMEP_g$: gross indicated mean effective pressure

LED: light emitting diode

MFB50: crank angle of 50% mass fraction burned

$SOC_{pilot/main}$: start of pilot/main combustion / heat release

SSE: start of solenoid energizing

TDC: top dead center

Appendix

Because imaging is performed through the piston, the raw images are distorted. The distortion pattern depends on both the crank angle and the location of the object of interest relative to the piston. While automatic distortion correction routines exist in commercial image capture software packages, they often require human intervention if the distortion becomes too extreme. A different approach to automated image distortion correction has been developed based on ray tracing. This approach takes advantage of the axisymmetric piston geometry (except for the valve cut-outs, which do not affect images of the fuel injection taken inside the bowl), so the problem of distortion correction is reduced to two dimensions (a radial dimension and a dimension parallel to the cylinder axis). The simulation of rays and their interaction with the piston is simulated with the methodology described below.

A ray is defined by its starting point and direction of propagation. The intersection of the ray's path and the first surface it will encounter is computed and the interaction of the ray with the surface simulated. Depending on the nature of the surface, the ray may be reflected, refracted, or absorbed. It is then transformed into a new ray (defined by its origin at the intersection and its new direction). Refraction is computed according to Snell's law [24].The ray is traced in this manner until it leaves the system. Cubic splined surfaces with continuous first derivatives define the two-dimensional piston perimeter (shown in Figure A - 1).

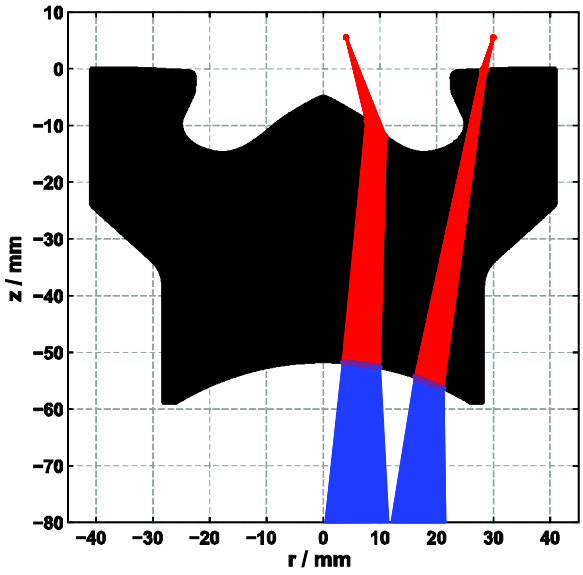

Figure A - 1: Ray bundles originating from two points in 2-D space above the piston and their paths through the piston towards the mirror

A fan of rays with their origins at a given point in space above the piston is defined, and each is traced until it leaves the system. The rays that determine the form of the distorted image are those that reach the piston mirror and camera. In the case of this simulation, these rays are assumed to be the ones that pass through a long (~250 mm) absorptive vertical tube (diameter 49.8 mm) located below the piston so that they reach the elliptical piston mirror (depicted in Figure 2). The ray bundles shown in Figure A - 1 represent the rays that leave from these two original points and reach the piston mirror. Rays leaving these points at any other angle will not reach the mirror. In other words, only rays that would reach the piston mirror are allowed to leave the system. Rays that intersect the side walls of the piston are absorbed. It is observed that the rays leaving the piston and reaching the turning mirror are divergent (shown by the bundles of rays leaving the bottom of the piston in Figure A - 1). Therefore, one or several virtual images are formed at the back-projected intersections of these rays with one another. In this way, a point in real space is mapped to a cloud of intersection points that are the virtual image of the original point. The virtual images of objects above the piston (calibration targets, liquid fuel, etc.) are what the camera "sees".

For crank angles near TDC and ray fan origins in or near the piston bowl, the virtual images that form are often confined to very small spaces, such that they can be represented by a single point with reasonable precision (typically better than 100 μm in the radial direction). For this work, a mapping between the real world and the virtual image is defined in this manner. A series of ray fans located at various points along a line inside the cylinder can be traced and represent the radial mapping function of a surface in real space. Once this mapping function is known, an image is distortion-corrected as follows:

1. The center of the cylinder is determined from the raw (distorted) image; this is performed manually, as the location of the center does not change from experiment to experiment.
2. The distance between the center point and each pixel (i.e. radius) in the raw image is computed.
3. The radii determined in step 2 are scaled by an empirically determined scaling factor (the ratio of distance in virtual image space to pixels in the captured images) to determine their magnitude (in mm).
4. The virtual image radii are used as inputs to the radial mapping function to yield undistorted radii.
5. The undistorted radii are scaled by a constant (8 pixels/mm) to determine the spatial scaling of the final image.

6. The pixels of the original image are moved into their new positions as defined by the undistorted radii (the angular position of each pixel remains unchanged).
7. A two-dimensional, bi-linear interpolation scheme is used to "fill in the blanks", that is the locations where no information is available after the initial pixel displacement procedure described in step 6.

It is observed that the distortion of a horizontal plane changes dramatically as the plane is moved parallel to the cylinder axis towards the piston pip. This is a problem when imaging the injection jets, as they are not oriented in a horizontal plane. Ray tracing is therefore performed for ray fans located along the theoretical jet axis (inclined by 15.5 ° to the cylinder head). An example of such a ray tracing simulation is depicted in Figure A - 2 for a limited number of ray bundles. The black dots indicate the locations of the virtual images of each point along the jet axis. Mapping functions generated in this manner are created for crank angles between 12 CAD BTDC and 30 CAD ATDC in increments of 2 CAD. The two dimensional mapping functions are combined in three-dimensional space (the dimensions are crank angle, virtual image radius, and undistorted radius) and a surface is fitted to them. This surface is used to determine the mapping function (via bilinear interpolation) for any arbitrary crank angle within this range. In this way, any image can be automatically distortion corrected if the crank angle at which it was taken is known.

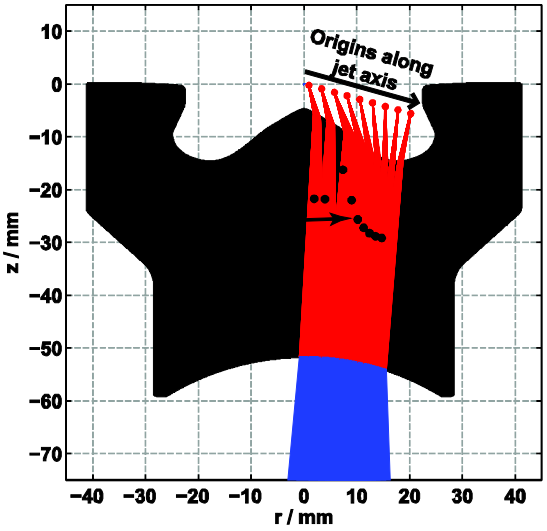

Figure A - 2: Example of ray tracing with ray bundle origins located along the injection jet axis and black dots to show the locations of virtual images

For this work, the distortion corrected images are scaled to a resolution of 8 pixels per mm along the jet axis. Testing of this procedure with calibration targets oriented along the jet axis indicate that it introduces an uncertainty in liquid length measurements of something on the order of 2 pixels, or 0.25 mm along the jet axis. However, any errors in liquid length measurements will be largely consistent between different cases, as the distortion correction is the same for a given crank angle. This facilitates comparison between images taken for various dwells.

Once the images in a sequence have been distortion corrected, steps are taken to isolate the injection jets from the background. For this work, the approximate median method described in [25] is used to model the background. This method relies on a sequence of images, which in this case are the sequences of 300 distortion corrected images for every injected cycle. The background model is initialized as the first image (taken at the start of solenoid energizing (SSE), at which point the injection has not yet started). For each subsequent image in the sequence, the background model is updated and a background subtracted image is created, then thresholded. This method effectively removes features attributed to the background, such as the valves and the injector tip. Finally, each jet's image data is isolated and processed individually. Liquid lengths are calculated according to the methods given in [17] with some subtle differences. Liquid lengths are initially computed from the images and are measured from the empirically determined center of the chamber (not the apparent origin of the jet, which cannot be adequately distinguished from the nozzle exits with the resolution provided by this system). The distance between the injector axis and the nozzle exits is subtracted from this distance. This length represents the projection of the true liquid length, which exists along the jet axis, onto a horizontal plane. The liquid lengths reported in this work are calculated by dividing this length by the cosine of 15.5 °. A threshold value of 3% of each jet's maximum intensity proved to be robust for all cases. Liquid lengths are calculated for each jet in each frame in every image sequence. An example of a distortion corrected, background-subtracted image is shown in Figure A - 3. The locations where the projected liquid length is computed are shown with small "+" symbols, and a large "+" is positioned at the center of the image.

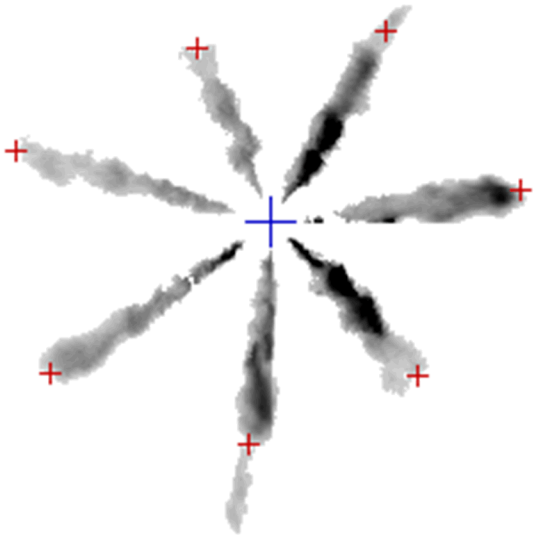

Figure A - 3: Distortion-corrected, background-subtracted image; displayed with an inverted grayscale color map, Intensity range: 0-512 counts, gamma correction = 0.7